Materials Today Communications 39 (2024) 108843

Contents lists available at ScienceDirect

Materials Today Communications

journal homepage: www.elsevier.com/locate/mtcomm

Laser-induced carbonization of Ni-BDC layer on PET: Functional upcycling of polymer wastes towards bend resistive sensor

Dmitry Kogolev [1,a], Ekaterina Kurtsevich [1,a], Maxim Fatkullin [a], Alexey Zinovyev [a], Alina Gorbunova [a], Raul D. Rodriguez [a], Olga Guselnikova [a,b], Rabah Boukherroub [c], Pavel S. Postnikov [a,d,*]

[a] Research School of Chemistry and Applied Biomedical Sciences, Tomsk Polytechnic University, Tomsk 6340034, Russian Federation
[b] Centre of electrochemical and surface technology, Viktor Kaplan Straße 2, Wiener Neustadt 2700, Austria
[c] Univ. Lille, CNRS, Univ. Polytechnique Hauts-de-France, IEMN, UMR CNRS 8520, Lille F-59000, France
[d] Department of Solid-State Engineering, University of Chemistry and Technology, Prague 16628, Czech Republic

ARTICLE INFO

Keywords:
Functional upcycling
Polyethylene terephthalate waste
Metal-organic framework
Laser-induced graphene
Bend resistive sensor
Internet of Things

ABSTRACT

The growing accumulation of waste polyethylene terephthalate (PET) presents a significant environmental challenge requiring the development of sustainable recycling methods. In this study, a novel approach for upcycling preliminary recycled waste PET into bend resistive sensors through laser-assisted carbonization of surface-grown Ni-BDC (BDC = 1,4-benzenedicarboxylate) has been proposed. The fabrication process involves the solvothermal formation of a homogeneous Ni-BDC layer, followed by treatment with a 405 nm laser system to create a graphene-like layer with enhanced conductivity (sheet resistance 6.2 ± 3.4 Ω per square). The developed sensor demonstrates remarkable robustness, a linear response in a wide bending angle range (6–44°), as well as excellent mechanical stability and stiffness. This contribution paves the way for the development of high-value materials from waste PET as a resource for applications in the Internet of Things, otherwise discarded materials.

1. Introduction

In response to the pressing challenges of climate change and the ever-increasing accumulation of polymer waste [1], the concept of functional upcycling has gained significant interest in environmental engineering. Functional upcycling aims at surface transformation of plastic waste in contrast to conventional chemical recycling or upcycling approaches, where bulk transformation of plastic requests more energy. Thus, the functional approach offers a cost-efficient avenue for designing innovative materials [2–9].

In the functional re-/upcycling of polymer waste, polyethylene terephthalate (PET) holds a unique position, mainly due to its inherent capacity for easy conversion of the polymer backbone into reactive groups [1]. PET has exceptional properties including mechanical and chemical stability, toughness, optical transparency, processability, and wide availability [10–15]. Despite these advantages for re-/upcycling, the ubiquity of PET enables to reach only 30% recycling rate [16]. In frame of functional upcycling strategy, PET can be transformed into terephthalic acid (TA), a main component of the extensive family of terephthalate-based metal-organic frameworks (MOFs) [17]. This transformation has become the origin for MOFs powder synthesis [18–24] and composite materials – PET coated by MOFs (PET@MOF) [25–30]. These composites found application as photocatalyst [27] and sorbents [26,28]. Later, this strategy was upgarded towards the preparation of conductive carbon-based materials *via* MOFs pyrolysis for energy-related applications [20,31–40]. However, previously reported approaches require significant energy consumption, an inert atmosphere, and post-processing to obtain the final device [20,33].

Recently, carbonization to graphene-like materials was improved by laser treatment of immobilized MOFs powders [41–44]. In these cases [41–44], the use of commercial TA-based ligands instead of readily available waste PET feedstock increases the cost of materials. Secondly, the performance of these functional materials does not meet modern requirements in terms of electrochemical capacitance [45],

* Corresponding author at: Research School of Chemistry and Applied Biomedical Sciences, Tomsk Polytechnic University, Tomsk 6340034, Russian Federation.
E-mail address: postnikov@tpu.ru (P.S. Postnikov).
[1] Equal contributors

https://doi.org/10.1016/j.mtcomm.2024.108843
Received 21 November 2023; Received in revised form 5 March 2024; Accepted 4 April 2024
Available online 5 April 2024
2352-4928/© 2024 Elsevier Ltd. All rights reserved.

overpotential of hydrogen [43,44] and oxygen [44] evolution reactions. This is probably due to poor mechanical strength and homogeneity of the resulting conductive layer [41,43–45]. Thus, in energy-related field the preparation of carbon-based functional materials with reasonable cost along with mechanical robustness and stable performance is a challenge.

Recently, a functional upcycling strategy for waste PET through laser-assisted processing of surface-grown terephthalate MOFs has been suggested [29]. Here, this strategy was built upon expanding to energy-related devices to create bending sensors directly from waste PET by a laser scribing procedure (Fig. 1). This novel sensor has impressive mechanical stability and stiffness, making it suitable for applications in construction and building. Moreover, the technological feasibility of this process opens the door to the broader development of waste PET-derived sensors.

2. Materials and methods

2.1. Materials and reagents

PET sheets from recycled plastic used as a starting material were purchased in a local store. All reagents and solvents were bought from Sigma-Aldrich and used without preliminary purification.

2.2. Methods

2.2.1. Fourier-transform infrared spectroscopy (FTIR)

FTIR spectra were recorded using IRAffinity-1S spectrometer (Shimadzu) equipped by ATR setup with diamond crystal. The spectra were registered with 2 cm^{-1} resolution and 1500 scans per spectrum. All spectra were adjusted using a baseline linearization in the range of 3300–550 cm^{-1}.

2.2.2. Ultraviolet-visible spectroscopy (UV–vis)

The absorbance spectra were recorded on Thermo Scientific Evolution 201 UV–visible Spectrophotometer. The samples were placed in a polytetrafluoroethylene cuvette for solid-state materials with a glass window. Spectra were registered in 350–1100 nm range with 2 nm resolution.

The band gap energies (E_g) of the Ni-BDC, PET@Ni-BDC, and PET@C were determined using the Tauc equation at the point of intersection of the approximate tangent to the linear part of the Tauc plots with the X axis:

$$\alpha \times h \times \nu = A \times (h \times \nu - E_g)^{n/2}. \quad (1)$$

Here α, h, ν, A, E_g represent the molar absorptivity, Planck's constant, light frequency, absorbance and band gap energy, respectively. The value of n for a semiconductor is determined by the type of junction ($n = 4$ for a direct junction and $n = 1$ for an indirect junction).

2.2.3. Raman spectroscopy

Raman spectra were registered by using Renishaw inVia Raman microscope with a green laser source (532 nm) with 90 scans and 1 s exposure time. The laser beam was focused on the sample using a 20× objective.

2.2.4. The four-point probe technique

MS Tech MST 4000 A microprobe station was used to arrange the tips in a square with a constant distance of 386 μm between probes.

Sheet resistance (R_{sh}) of the PET@C materials was determined using the four-point probe technique in a square configuration according to the Eq. (2):

$$R_{sh} = (2 \times \pi / \ln 2) \times (U/I). \quad (2)$$

Here U and I correspond to applied voltage and current, respectively.

2.2.5. Optical images

Optical images were taken using Leica S9i microscope using a 2× objective.

2.2.6. X-ray diffraction (XRD)

The crystal structure of the samples was studied by XRD using Powder X-ray diffractometer XRD-7000S (Shimadzu, Japan) in the scanning range of 6.3–80° using a CuKα source (30 mA, 40 kV, and 1 nm slit) in the Bragg-Brentano configuration.

2.2.7. X-ray photoelectron spectroscopy (XPS)

The XPS spectra were recorded on a Thermo Fisher Scientific XPS NEXSA spectrometer equipped with an Al K Alpha X-ray monochromatic emitter with an energy of 1486.6 eV. Survey spectra were recorded using radiation with an energy of 200 eV and an energy resolution of 1 eV. High-resolution spectra were collected using radiation with an energy of 50 eV and a resolution of 0.1 eV. The analysis area was 200 μm^2. A flood gun was used to compensate charges. A monatomic gun was used for depth profiling with an energy of 4000 eV.

2.2.8. Scanning electron microscopy with energy dispersive X-ray analysis (SEM–EDX)

The images were taken on a Tescan MIRA 3 LMU instrument in the reflected electron diffraction mode. The instrument was equipped with an Oxford Instrument Ultim Max 40 energy-dispersive X-ray device. All samples were coated with a carbon layer by magnetron sputtering. Scanning was performed using an accelerating voltage of 20 kV. Samples for cross section images were prepared by freezing in liquid nitrogen and cutting with scissors.

2.2.9. Mechanical tests

The Young's module was determined using Gotech AI-7000 M universal testing machine equipped by pneumatic grips. Tests were performed with traverse speed of 10 mm per min.

2.2.10. Bend sensor tests

Resistance response to bending was studied with a three-point flexural test using 300 mm^2 engraved meander-shaped sample. The distance

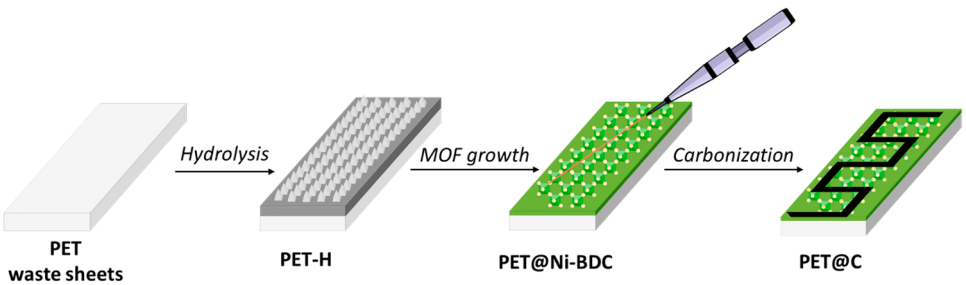

Fig. 1. Strategy for PET@C preparation from PET waste *via* PET hydrolysis, Ni-BDC PET surface growth, and laser scribing process by 405 nm irradiation.

between the two side points was fixed to 20 mm. The middle point movement was controlled by a micro-step motor. A constant current was applied to the sample, and a voltage drop during bending cycles were observed by potentiostat-galvanostat P45-X, then resistance was calculated by Ohm's law. The same conditions were used for cyclic bending at the bending angle of 11°. Bending under a certain angle was conducted on three samples.

All measurements were triplicated in order to present data with standard deviation calculated according to the Eq. (3):

$$\sigma = \sqrt{\frac{\Sigma(x_i - \mu)^2}{N}} \quad (3)$$

Here σ – the standard deviation, x_i – the value of a single sample value, μ – the arithmetic mean of the sample, N – the sample size.

3. Results and discussion

3.1. Preparation of PET@Ni-BDC

The investigation originated from the development of a rational approach towards creating a hybrid material with surface-grown Ni-BDC (where BDC = 1,4-benzenedicarboxylate) MOFs, primarily due to the cost advantages of this method compared to UiO-66 (Fig. 2A). To achieve this, recently reported method was adapted for the hydrolysis of waste PET by acid treatment followed by the solvothermal growth of MOFs [29]. As a source of waste PET, plates derived from post-consumer waste for building applications were used. The used plates are a typical waste material potentially containing additives or degraded species [46]. The development of upcycling procedure on target waste source instead of virgin PET is crucial due to the potential reactivity difference. In the first step, waste PET sheets were washed and cut into 1.0 × 3.0 cm^2 pieces. These prepared wafers underwent surface hydrolysis by concentrated sulfuric acid to introduce –COOH groups onto the PET surface, which are essential for subsequent surface-assisted nucleation with nickel ions (Section 1, ESI†). The formation of –COOH groups was confirmed by FTIR spectroscopy and XPS, with additional details provided in Section 1, ESI†.

The activation of the waste PET surface during hydrolysis allowed for the direct growth of Ni-BDC MOF on the wafers. A previously published method was adapted to synthesize Ni-BDC under solvothermal conditions by mixing a nickel precursor with terephthalic acid derived from waste PET bottles [22] in *N*,*N*-dimethylformamide (DMF) (details are provided in Section 2, ESI†) [47]. Initially, conventional method that involves 15 hours of heating was tested (Section 2, ESI†) [47].

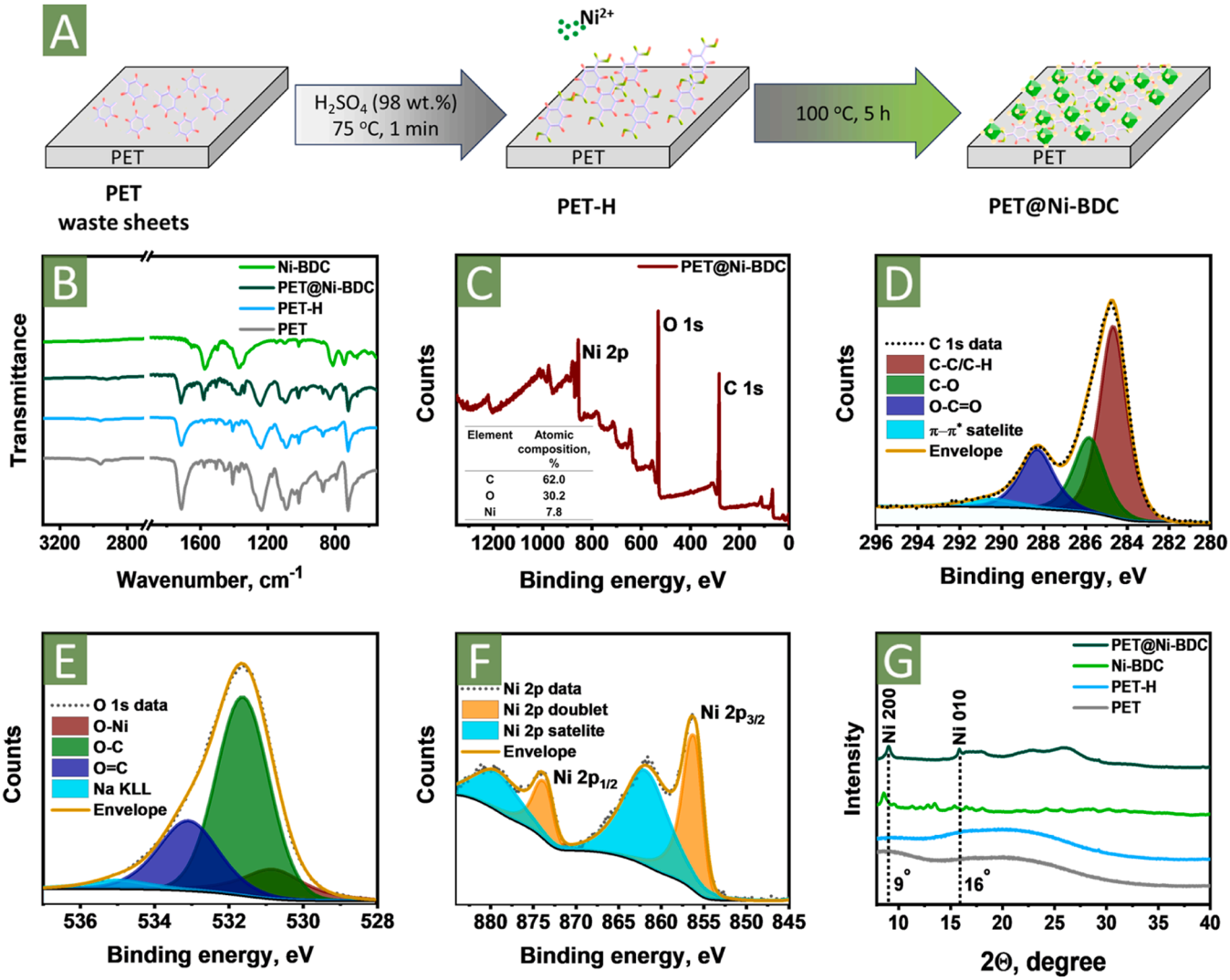

Fig. 2. (A) Scheme of PET@Ni-BDC preparation *via* PET hydrolysis and Ni-BDC growth. (B) FTIR spectra of pristine and hydrolyzed PET, PET@Ni-BDC, and Ni-BDC powder. Characterization of PET@Ni-BDC by XPS: (C) survey spectrum and core level spectra of (D) C 1 s, (E) O 1 s, and (F) Ni 2p. (G) XRD patterns of pristine (grey), hydrolyzed (blue), coated by Ni-BDC PET sheets (olive), and Ni-BDC (green).

Unfortunately, this led to the formation of thick, detached, and inhomogeneous Ni-BDC layers, which could negatively affect the subsequent laser-induced carbonization (Fig. S5A and B, ESI†). To overcome this issue, the precursor loading was decreased by half, but unfortunately, the same issues persisted (Fig. S5C and D, ESI†). Finally, the preparation of the desired PET@Ni-BDC material by optimizing the reaction time was achieved. The formation of a uniform thin layer of Ni-BDC on the hydrolyzed PET surface was observed after just 5 hours of heating (Fig. S5E and F, ESI†). The final optimized procedure includes the growth of Ni-BDC directly on hydrolyzed PET sheets under solvothermal conditions. It is worth noting that a reduced amount of reagents and processing time was applied, making the process more economically and energetically efficient.

3.2. Characterization of PET@Ni-BDC

The formation of the Ni-BDC layer on PET sheets was confirmed by a series of spectroscopic analyses. FTIR spectra of pristine, hydrolyzed PET, PET sheets coated by Ni-BDC, and Ni-BDC powder are presented in Fig. 2B. In the spectrum of pristine PET, the characteristic peaks at 1712 and 1240 cm^{-1} associated with C═O bonds were observed (see full peak assignment in Table S1, ESI†). After hydrolysis, a broad peak at 3180–3380 cm^{-1} (Fig. S2, ESI†) confirming the presence of –COOH groups on the surface (Fig. 2B) was observed [48,49]. Following the growth of Ni-BDC on PET, characteristic peaks corresponding to COO–Ni groups were detected, which exhibited symmetric (1366 cm^{-1}) and asymmetric (1582 cm^{-1}) vibrations of COO^- (Fig. 2B) [50]. The FTIR data of PET@Ni-BDC is in agreement with that of Ni-BDC powder and previously published data (Table S2, ESI†) [51].

The chemical compositions of PET@Ni-BDC and intermediate products was studied by XPS (Fig. 2C-F). The hydrolysis of PET resulted in an increase in the C═O component intensity on the O 1 s deconvoluted peak (533.0 eV, Fig. S4C and F, ESI†) due to the formation of –COOH groups. The subsequent growth of Ni-BDC led to drastic changes in the surface chemical composition. The XPS survey scan revealed the appearance of a Ni^{2+} related peak (Fig. 2 C), indicating the presence of 7.8 at% of Ni [52]. The C 1 s peak deconvolution showed the same chemical state as PET and PET-H (Fig. 2D and S4B and E, ESI†). However, on the O 1 s deconvoluted peak, the appearance of the O–Ni component at 530.8 eV was observed, along with a notable decrease in the O═C component intensity (533.1 eV, Fig. 2E).

In the high-resolution Ni region spectrum, Ni $2p_{3/2}$ at 856.1 eV and Ni $2p_{1/2}$ at 873.6 eV peaks were identified, along with corresponding shake-up satellites attributed to the Ni $2p_{3/2}$ at 861.8 eV and Ni $2p_{1/2}$ at 879.3 eV of Ni^{2+} (Fig. 2 F) [52]. The localization of Ni-related peaks is in good agreement with the high-resolution spectra of Ni-BDC powder (Fig. S6D, ESI†).

The crystallinity of the materials was evaluated using XRD (Fig. 2 G). PET and hydrolyzed PET showed an amorphous structure without well-distinguishable reflections (Fig. 2 G) [29,53]. However, after the growth of Ni-BDC, discernable diffractions at 9 and 16° was observed, corresponding to Ni-BDC [54], confirming the formation of the PET@Ni-BDC composite (Fig. 2 G).

The surface morphology of prepared materials and distribution of Ni-BDC crystallites across the material's surface were investigated by SEM–EDX analysis (Fig. 3A-D). Pristine PET exhibited a smooth surface

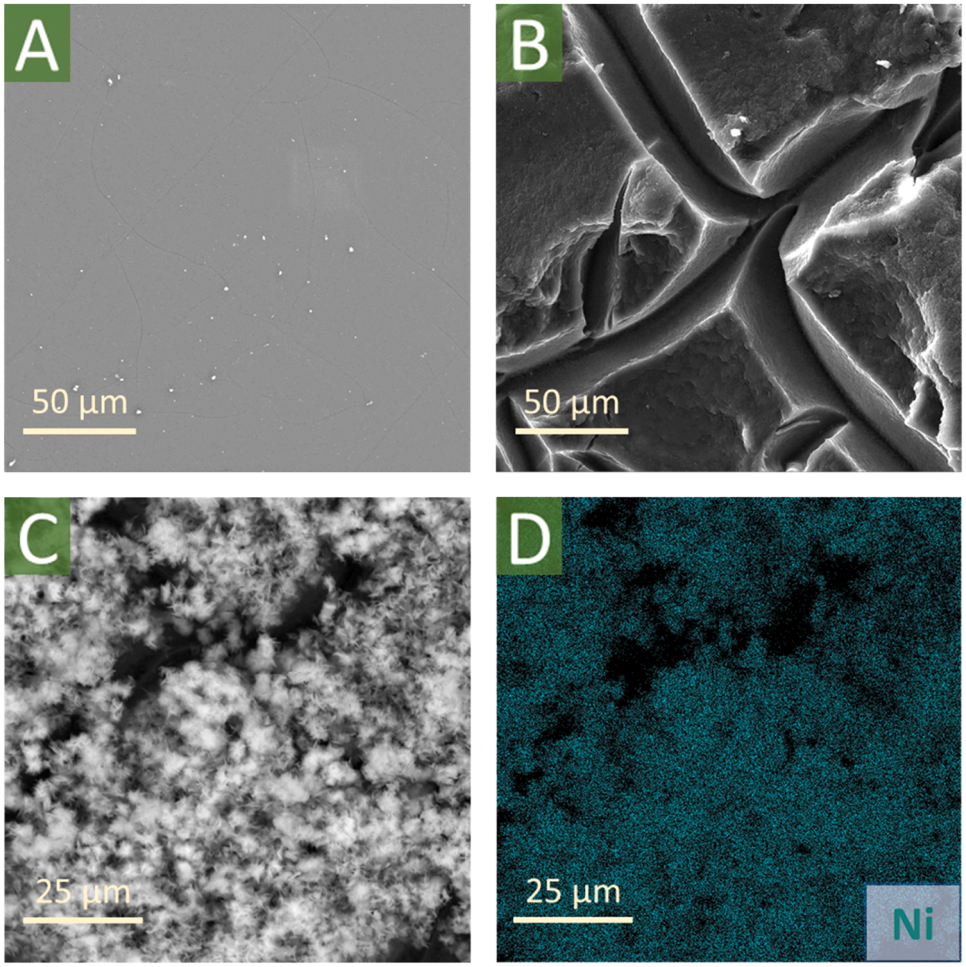

Fig. 3. SEM images of (A) pristine PET sheets, (B) hydrolyzed PET sheets, and (C) PET@Ni-BDC. (D) SEM–EDX map of Ni across PET@Ni-BDC.

without significant defects or features (Fig. 3A). Hydrolysis led to the formation of clearly visible cracks and cavities across the whole surface (Fig. 3B). Surface-assisted growth of Ni-BDC resulted in drastic changes in surface morphology, with cracks and features uniformly covered by Ni-BDC crystallites (Fig. 3C). The MOF layer was composed of ultrathin nanosheet arrays densely packed into irregular particles with an average size of ~2.5–3.0 μm, consistent with the shape of Ni-BDC crystals prepared by the same method (Fig. S7A and B, ESI†). EDX mapping results confirmed the homogeneous nickel distribution with a relatively high Ni concentration (approx. 23.6%) as shown in Table S3, ESI† (Fig. 3D). This value is similar to the Ni concentration of pure Ni-BDC (Fig. S8 and Table S4, ESI†) additionally confirming the Ni-BDC formation.

3.3. Laser-induced carbonization of PET@Ni-BDC

The next crucial step of the strategy for PET waste functional upcycling was the laser treatment of the PET@Ni-BDC surface to generate the PET@C composite (Fig. 4 A and B). The absorbance spectrum of PET@Ni-BDC was recorded to determine the optimal laser wavelength for the treatment (Fig. 4C). Notably, the main absorbance maximum at 395 nm was not observed for pristine or hydrolyzed PET (Fig. S3, ESI†). This absence indicated the potential for selective carbonization of the MOF layer without significant interaction between the laser beam and non-functionalized PET. Based on the absorbance spectra, a 405 nm light-emitting diode (LED) source (pulse frequency = 1.6 kHz, power = 1500 mW) were chosen to be integrated into a commercially available NEJE DK-8-KZ laser engraving system. This choice offered several advantages over traditional femtosecond lasers, including availability, cost-effectiveness, and the capability to process a larger area of material [55].

In the first laser processing experiment on PET@Ni-BDC, a laser beam with a movement speed of 9.9 mm per s and an irradiation power of 600 mW was tested [29]. The laser path is schematically illustrated in Fig. S9, ESI†. The selective carbonization of PET@Ni-BDC was observed at the point of contact between the laser beam and the material's surface. After the laser treatment, a uniform black layer on the PET surface showed a low sheet resistance of 14.0 ± 2.9 Ω per square, indicating its potential applicability as a bending sensor.

To further optimize the laser processing conditions, the Nelder-Mead method was employed, varying the laser power and laser movement speed (Fig. 4D, Table S5; see Section 3, ESI† for details). Surface resistance serves as a crucial indicator of carbonization efficiency, reflecting the uniformity of the carbon layer and the potential applicability of the resulting material. The optimization originated from selecting three random points in a triangular parametric shape to adjust two laser parameters (points 1–3, Fig. 4D). Then conductivity values were measured

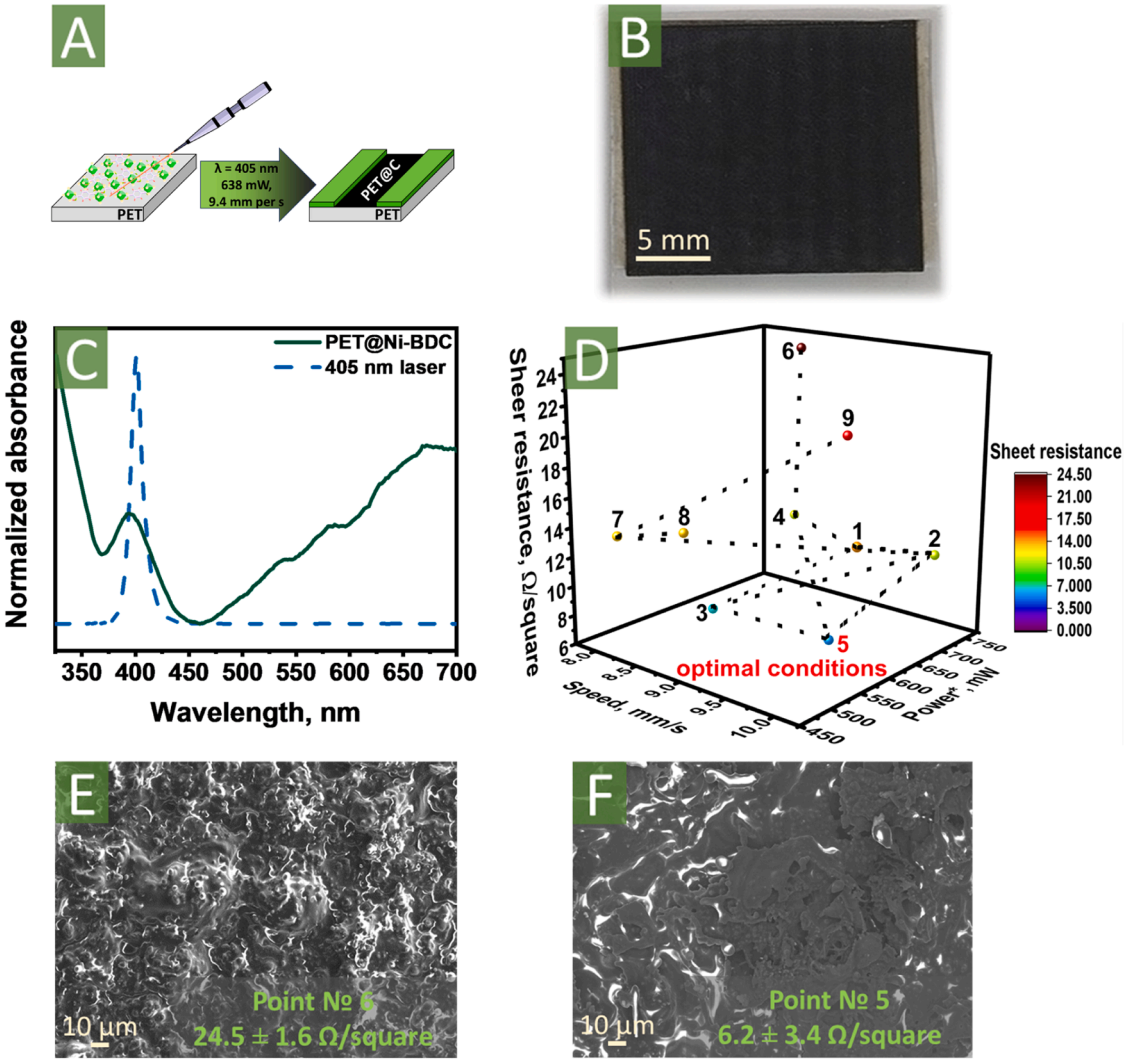

Fig. 4. (A) Scheme of PET@Ni-BDC laser treatment. (B) PET@C image. (C) UV–vis spectra of PET@Ni-BDC (the dashed line represents the excitation wavelength of 405 nm laser). (D) Optimization of PET@Ni-BDC laser treatment by Nelder-Mead method. *Nominal laser power. SEM image of PET@C after laser treatment under starting (E) and optimal (F) conditions.

at the vertices of the triangle, and operations like reflection, compression, and stretching of the triangle were performed. The top with the lowest conductivity was significantly reduced in electrical resistance. Consequently, the formation of a rough surface gave a relatively high sheet resistance of 24.5 ± 1.6 Ω per square (Fig. 4E). Through this optimization process, a considerable reduction in sheet resistance to 6.2 ± 3.4 Ω per square was achieved (Fig. 4 F). Thus, the optimal conditions were determined as a laser beam scanning at a speed of 9.4 mm per s with a laser power of 638 mW. It is worth noting that the PET@C material, obtained through this optimization, exhibited one of the highest electrical conductivities among similar graphene-based coatings prepared by laser treatment (Table 1).

3.4. Characterization of PET@C

The PET@C material, prepared under optimized conditions, was characterized by Raman spectroscopy. After the laser treatment of PET@Ni-BDC, spectral features associated with the Ni-BDC structure (1133, 1172, 1424, 1555, and 1724 cm^{-1}) disappeared (Fig. 5A). Instead, the Raman spectrum of PET@C revealed distinctive peaks at 1350 and 1583 cm^{-1}, attributed to the D and G peaks of graphene-like materials [71]. The presence of few-layered graphene sheets impregnating the polymer matrix was evidenced by the characteristic 2D mode fingerprint at 2699 cm^{-1}. Furthermore, the relatively high-intensity ratio (I_D/I_G = 0.96) indicated a high graphitization degree, explaining the material's low sheet resistance.

The full conversion of the Ni-BDC layer was confirmed by FTIR. After treatment, Ni-BDC-related vibration bands (symmetric and asymmetric stretch vibrations of COO–Ni bonds at 1366 and 1582 cm^{-1}, respectively) disappeared (Fig. S10 and Table S6, ESI†). However, the characteristic bands of PET remained visible, confirming the formation of the composite material, with PET as a matrix and carbonized Ni-BDC as the filler.

The full conversion of Ni-BDC crystals was further evidenced by XRD, demonstrating the disappearance of Ni-BDC characteristic peaks at 9 and 16° (Fig. 5B) [54]. At the same time, the peak at 43° suggested the formation of Ni_3C (Fig. 5B, insert) [72]. Generally, the formation of metal carbides during the carbonization of MOFs was observed recently by our group [29] and Deng's group [73], and also in laser processing of Al nanoparticles on PET [74].

The chemical composition of PET@C was analyzed by XPS (Fig. 5C,F and S11A-C, ESI†). The survey scan revealed changes in surface element concentrations, with an increase in carbon (from 62.0 to 82.1 at%), a decrease in oxygen (from 30.2 to 17.9 at%), and the disappearance of nickel (Fig. 5C and F). The C 1 s peak deconvolution confirmed the presence of the sp^2 hybridization component (283.3 eV) in addition to the C–C/C–H species, differentiating PET@C from PET@Ni-BDC (Fig. S11A, ESI†). These results evidenced the formation of laser-induced graphene along with fused PET upon laser treatment, in agreement with Raman spectroscopy results. The O 1 s core level spectrum revealed the disappearance of the O–Ni component, a decrease in the O–C component, and an increase in the O═C component intensity (Fig. S11B, ESI†). Surprisingly, no Ni-related peaks were observed during the initial analysis of PET@C due to the limited XPS penetration depth of just a few nanometers and the Ni distribution after laser scribing (Fig. S11C, ESI†).

To overcome this depth limitation, a monatomic Ar^+ depth-profiling technique was used to etch the surface, followed by XPS analysis (Fig. 5C,D and F and S11D and E, ESI†). The survey scan revealed a sufficient increase in carbon (from 82.1 to 98.1 at%) and a decrease in oxygen concentrations (from 17.9 to 1.4 at%) implied the decomposition of the organic ligands into graphitic carbon [44], along with the appearance of nickel (0.5 at%) (Fig. 5C and F). The C 1 s peak deconvolution showed the disappearance of the C–C/C–H components, and a significant decrease in the C═O band (Fig. S11D, ESI†). On the O 1 s deconvoluted peak, all component intensities decreased considerably. (Fig. S11E, ESI†). The presence of Ni $2p_{3/2}$ at 853.5 eV and Ni $2p_{1/2}$ at 870.8 eV peaks indicated the formation of nickel carbide in the resulting material (Fig. 5D) [75].

Furthermore, UV–vis spectroscopy showed increased absorbance throughout the visible region compared to Ni-BDC and PET@Ni-BDC (Fig. 5E). The band gap (E_g) underwent significant changes due to the formation of graphene-like domains (Fig. S12, ESI†), as reported previously for MOFs carbonization [76]. In this case, the value of E_g for PET@C was calculated as 0.406 eV (Fig. S12C, ESI†), which is much less compared to Ni-BDC MOF (2.980 eV, Fig. S12A, ESI†) and PET@Ni-BDC (3.037 eV, Fig. S12B, ESI†). These changes suggest the generation of a material with potential applications in solar desalination, solar photodegradation of pollutants, solar atmospheric water harvesting, *etc.* [77].

Morphological analysis of the PET@C composite through SEM–EDX (Fig. 6A and B) revealed drastic changes in PET@Ni-BDC surface morphology after laser treatment. Microcrystalline Ni-BDC structures

Table 1
Sheet resistance comparison of untreated and reduced GO and graphene materials produced by laser-induced carbonization.

Materials and methods	Laser information	Applied power	Sheet resistance, Ω per square	References
Pristine GO	–	–	10^6–10^{10}	[56–58]
Deposition of GO on a cotton fabric followed by reduction by hot press	–	–	900	[59]
Laser-induced graphene on polyimide	CO_2 laser	13 mW per cm^2	733–1100	[60]
Laser-induced graphene on polyimide	UV laser, 355 nm, pulse frequency 150 kHz, scanning speed of 50 mm per s	3 W	$1.5{\cdot}10^2$–$3{\cdot}10^5$	[61]
Laser-induced graphene on polyimide	UV pulsed laser, 355 nm, pulse frequency 30 kHz	–	0.44	[62]
Laser-induced graphene on polyimide	CO_2 laser, 365 nm, scanning speed of 1 mm per s	4.7–7.0 mW	15	[63]
Laser-reduced graphene oxide in liquid nitrogen environment	Picosecond pulsed laser: 1064 nm, pulse duration 10 ps, 100 kHz repetition rate, spot size 30 μm	–	50–60	[64]
Laser direct patterning of reduced GO on flexible (PET) substrate by femtosecond pulses	Femtosecond 515 nm laser, 280 fs pulse length, 500 kHz repetition rate	35–45 nJ pulse energy with 10–20 pulses per μm	200.0	[65]
Polyimide surface carbonization	CO_2 laser	4.5–8.25 W	60.0	[66]
Polyimide surface carbonization	CO_2 with 10.6 μm wavelength and a beam size of 0.127 mm	25 W	30 ± 2.6	[67]
Poly (Ph-ddm)-surface carbonization	CO_2 laser 10.6 μm, pulse frequency is 20 kHz	20 W	35.0	[68]
Laser-induced graphitization of ink based on cellulose and lignin	CO_2 laser 10.6 μm	3.3 W	3.8 ± 0.1	[69]
Carbonization of MOFs powder (LIC-(ZIF-8) and LIC-(ZIF-67))	CO_2 laser 1064 nm	4.8 W	Approximately 125	[42]
Low-cost laser carbonization (LIMPc)	450 nm LED pulse laser	580 mW	181	[70]
Low-cost laser carbonization (PET@LB-UiO-66)	405 nm LED pulse laser	735 mW	10.4 ± 3.1	[29]
Low-cost laser carbonization (PET@C)	405 nm LED pulse laser	638 mW	6.2 ± 3.4	This work

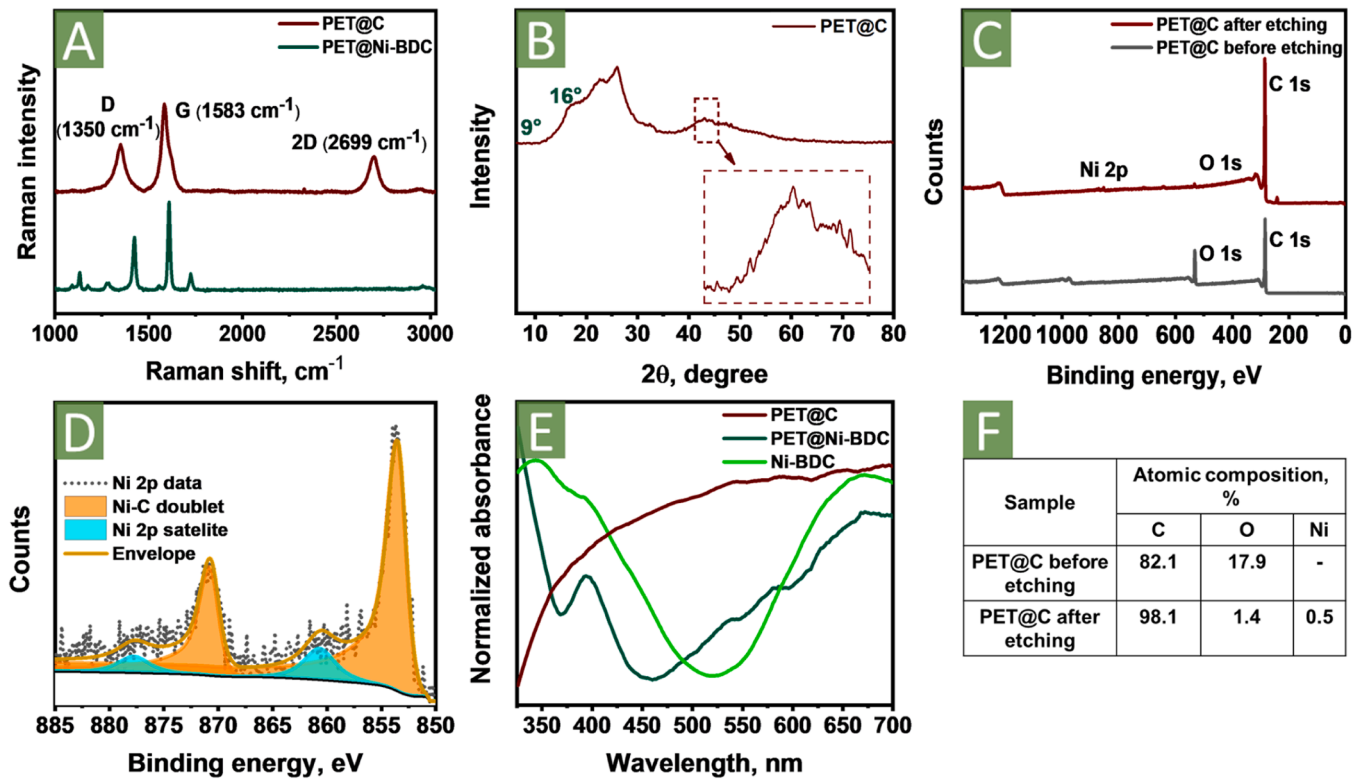

Sample	Atomic composition, %		
	C	O	Ni
PET@C before etching	82.1	17.9	-
PET@C after etching	98.1	1.4	0.5

Fig. 5. Characterization of PET@C: (A) Raman spectra, (B) XRD patterns, XPS: (C) survey spectra before and after Ar^+ surface etching, and (D) core level spectrum of the Ni 2p region after Ar^+ surface etching, (E) UV–vis spectra, (F) atomic composition table from (C).

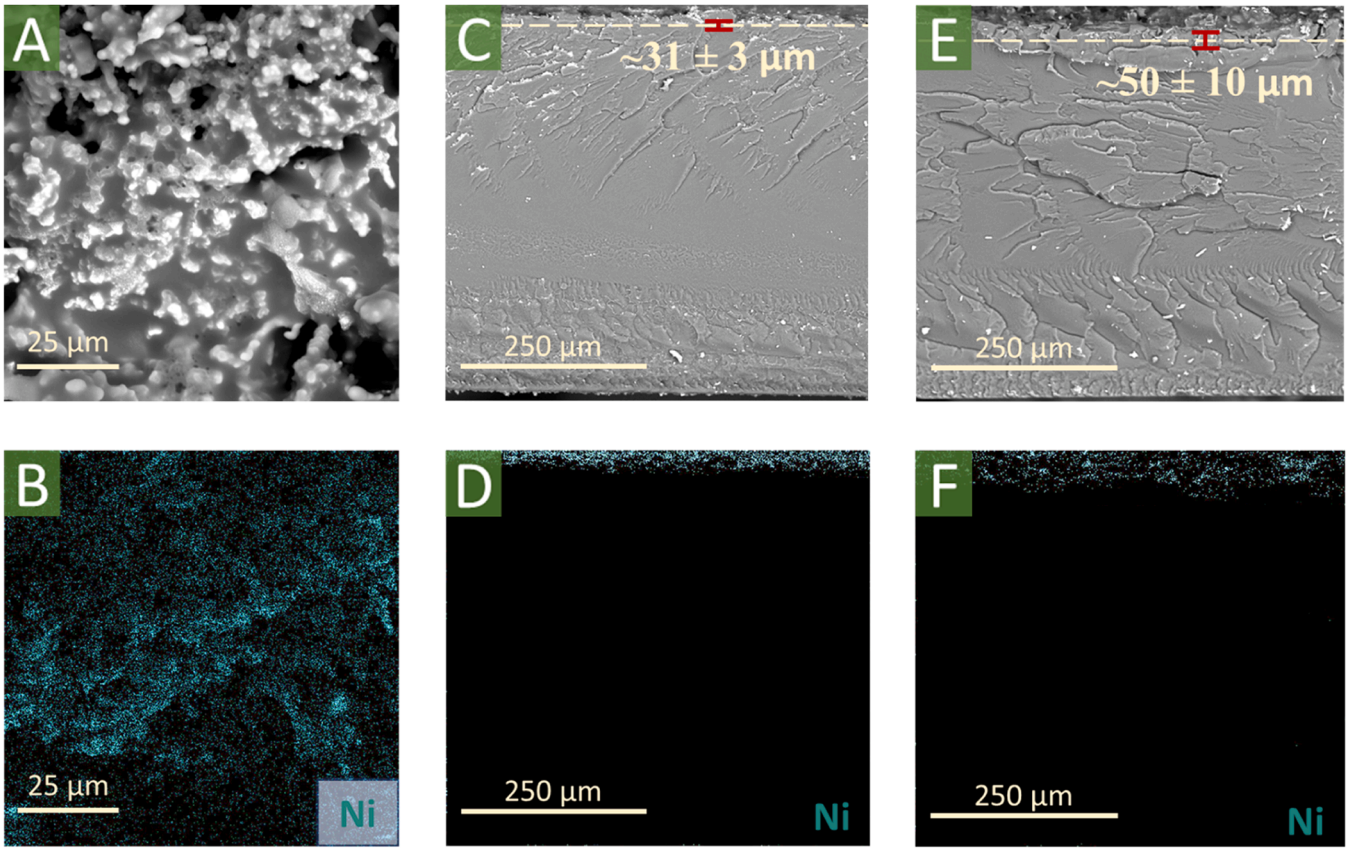

Fig. 6. Morphology investigation of PET@C: (A) SEM image, (B) EDX mapping of Ni. Cross-sectional SEM–EDX images of (C,D) PET@Ni-BDC and (D,F) PET@C.

transformed into a relatively smooth porous surface (Fig. 6A). The formation of pores resulted from the release of CO_2 during the decarboxylation of terephthalates [55]. EDX analysis of the treated surface revealed a homogenous distribution of Ni across the entire surface without significant particle agglomeration (Fig. 6B).

SEM combined with EDX analysis were applied to evaluate the thickness and Ni_3C distribution in the carbonized layer. The composite thickness measured approximately 50 ± 10 μm, which is larger than the thickness of the Ni-BDC layer (31 ± 3 μm). This observation aligns with a general mechanism similar to observed for UiO-66 [29], indicating a common process for PET@MOFs carbonization. This process involves the complex interplay of secondary melting of PET with the simultaneous formation of the composite (Fig. 6C and E). Moreover, the formation of pores throughout the composite layer was clearly observed (Fig. S13, ESI†). EDX analysis showed a concentration of Ni on the top layer for PET@Ni-BDC (Fig. 6D). In contrast, PET@C exhibited a relatively homogenous distribution of Ni in the vertical direction, suggesting the embedding of particles during the melting of the PET matrix (Fig. 6F).

3.5. Testing of PET@C as a bending resistive sensor

The next step was to study the possibility of using the PET@C material as the active component of a flexible resistive sensor (Fig. 7A). The resistance response to bending was investigated using a three-point flexural test (Fig. S14, ESI†). This test was performed on an engraved meander-shaped sample, which was manipulated by a micro-step motor. Throughout the test, a constant current was applied to the sample. Concurrently, the voltage drop experienced during the bending cycles was meticulously recorded. Subsequently, the resistance was calculated using Ohm's law based on these voltage measurements. The bending sensor exhibited a clear, distinguishable, and reproducible response to bending angles. As the bending angle increased, a corresponding increase in relative resistance changes $\Delta R/R_0$, demonstrating a linear response of 32 ± 1% up to 44° was recorded (Fig. 7B and S15, ESI†). Moreover, the sensor performance was tested under 1000 bending cycles at the bending angle of 11°, simulating long-term use for online monitoring in wearables and Internet of Things (IoT) applications (Fig. 7C). The sensor's response remained stable during the whole test, with only a ~3% difference between the starting point and the end of the long-term durability tests, indicating the sensor's robustness and stability during cycling bending (Fig. 7C, insert). To assess the mechanical properties and durability of the PET@C composite, tensile strength tests were applied (Fig. 7D). Ultimate tensile strength (UTS) was evaluated at a strain rate of 10 mm per min. The UTS of PET@C significantly increased from 38.2 to 57.1 MPa, with the same elongation of 5.4% compared to pristine PET (Fig. 7D). This enhancement can be attributed to PET surface melting during laser-induced transformations of surface-grown Ni-BDC and formation of the carbon-based material composite [78].

These findings suggest the potential use of the PET@C composite as a flexible resistive sensor, with promising applications in smart wearable devices [40,79,80], personalized health monitoring [81], electronic skin [82], human-machine interfaces [83], and more.

4. Conclusion

In summary, an experimental strategy was suggested for the functional upcycling of waste PET into bend resistive sensors, offering a

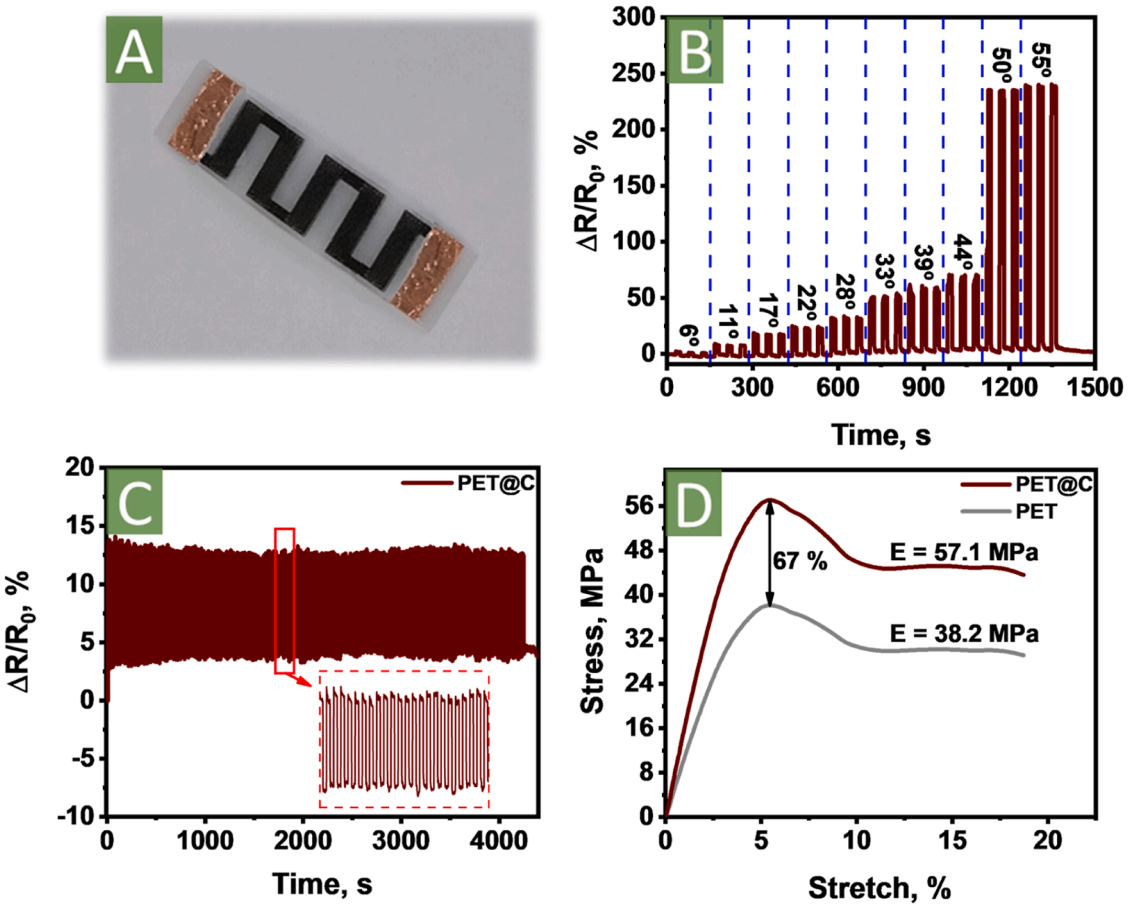

Fig. 7. (A) Image of the sensor. Resistive characterization of the PET@C bending sensor: (B) resistance response to the bending depth and (C) long-term durability testing for 1000 stretching and releasing cycles. (D) Ultimate tensile strength measurements of PET and PET@C.

sustainable solution to address the plastic waste problem. Our findings allow to achieve the following results. Firstly, by repurposing PET, a readily available and inexpensive material, it was successfully transformed into a value-added bend sensor. The developed approach efficiently transforms an abundant and low-cost material into a high-value bend sensor with several notable characteristics. Secondly, the fabrication process comprises a two-step sequence: first, the growth of Ni-BDC on the PET surface, and second, the laser-induced carbonization to create a conductive graphene/nickel carbide layer. Specifically, the sensors exhibit a low sheet resistance of $6.2 \pm 3.4\ \Omega$ per square, a robust and linear response across bending angles ranging from 6 to 44°, and commendable mechanical stability and stiffness. This results in a composite material display outstanding electrical conductivity and mechanical properties, particularly sensitive to bending forces, making it suitable for diverse applications in wearable electronics, robotics, and healthcare monitoring systems. Thirdly, the limitations of the current synthesis protocol include the use of hazardous chemicals and high-temperature processing that may raise environmental and safety concerns. Therefore, further steps will be made forward with milder hydrolysis experimental protocol and adaptation of suitable MOFs synthesis procedure on PET surfaces.

Overall, while this research marks a significant advancement in the functional upcycling of PET, it also opens avenues for future investigations to refine and scale the technology. The prospects of integrating such sensors into commercial applications are promising, and forthcoming studies will aim to address the current limitations, striving for greener synthesis routes and broader application scopes.

CRediT authorship contribution statement

Dmitry Kogolev: Writing – original draft, Validation, Methodology, Investigation, Conceptualization. **Maxim Fatkullin:** Methodology, Investigation, Conceptualization. **Ekaterina Kurtsevich:** Validation, Methodology, Investigation, Data curation. **Alexey Zinovyev:** Methodology, Investigation. **Raul D. Rodriguez:** Writing – review & editing, Validation, Resources. **Alina Gorbunova:** Methodology, Investigation, Formal analysis. **Rabah Boukherroub:** Writing – review & editing, Funding acquisition, Conceptualization. **Olga Guselnikova:** Writing – review & editing, Validation, Methodology, Data curation. **Pavel S. Postnikov:** Writing – review & editing, Writing – original draft, Supervision, Resources, Project administration, Conceptualization.

Declaration of Competing Interest

The authors declare that they have no known competing financial interests or personal relationships that could have appeared to influence the work reported in this paper.

Data Availability

Data will be made available on request.

Acknowledgements

The authors thank the central laboratories of TPU (Analytical center) for XPS measurements and Tomsk Regional Core Shared Research Facilities Center of National Research Tomsk State University and Science Park of St. Petersburg State University for SEM investigations. The research has been financially supported by the Ministry of High Education and Science of Russian Federation N⁰ 075–15–2022–244 (Russian-French project in the frame of PHC ‘‘Kholmogorov’’).

Appendix A. Supporting information

Supplementary data associated with this article can be found in the online version at doi:10.1016/j.mtcomm.2024.108843.

References

[1] O. Guselnikova, O. Semyonov, E. Sviridova, R. Gulyaev, A. Gorbunova, D. Kogolev, A. Trelin, Y. Yamauchi, R. Boukherroub, P. Postnikov, “Functional upcycling” of polymer waste towards the design of new materials, Chem. Soc. Rev. 52 (2023) 4755–4832, https://doi.org/10.1039/D2CS00689H.
[2] M. Jiang, X. Wang, W. Xi, H. Zhou, P. Yang, J. Yao, X. Jiang, D. Wu, Upcycling plastic waste to carbon materials for electrochemical energy storage and conversion, Chem. Eng. J. 461 (2023) 141962, https://doi.org/10.1016/j.cej.2023.141962.
[3] C. Jehanno, J.W. Alty, M. Roosen, S. De Meester, A.P. Dove, E.Y.-X. Chen, F. A. Leibfarth, H. Sardon, Critical advances and future opportunities in upcycling commodity polymers, Nature 603 (2022) 803–814, https://doi.org/10.1038/s41586-021-04350-0.
[4] H. Chen, K. Wan, Y. Zhang, Y. Wang, Waste to wealth: chemical recycling and chemical upcycling of waste plastics for a great future, ChemSusChem 14 (2021) 4123–4136, https://doi.org/10.1002/cssc.202100652.
[5] B. von Vacano, H. Mangold, G.W.M. Vandermeulen, G. Battagliarin, M. Hofmann, J. Bean, A. Künkel, Sustainable design of structural and functional polymers for a circular economy, Angew. Chem. Int. Ed. 62 (2023), https://doi.org/10.1002/anie.202210823.
[6] B. Wang, Y. Wang, S. Du, J. Zhu, S. Ma, Upcycling of thermosetting polymers into high-value materials, Mater. Horiz. 10 (2023) 41–51, https://doi.org/10.1039/D2MH01128J.
[7] Ł. Zedler, S. Wang, K. Formela, Ground tire rubber functionalization as a promising approach for the production of sustainable adsorbents of environmental pollutants, Sci. Total Environ. 836 (2022) 155636, https://doi.org/10.1016/j.scitotenv.2022.155636.
[8] H. Jung, G. Shin, H. Kwak, L.T. Hao, J. Jegal, H.J. Kim, H. Jeon, J. Park, D.X. Oh, Review of polymer technologies for improving the recycling and upcycling efficiency of plastic waste, Chemosphere 320 (2023) 138089, https://doi.org/10.1016/j.chemosphere.2023.138089.
[9] Z. Chen, W. Wei, B.-J. Ni, H. Chen, Plastic wastes derived carbon materials for green energy and sustainable environmental applications, Environ. Funct. Mater. 1 (2022) 34–48, https://doi.org/10.1016/j.efmat.2022.05.005.
[10] M.N. Ezzat, Z.T.A. Ali, Green approach for fabrication of graphene from polyethylene terephthalate (PET) bottle waste as reactive material for dyes removal from aqueous solution: batch and continuous study, Sustain. Mater. Technol. 32 (2022) e00404, https://doi.org/10.1016/j.susmat.2022.e00404.
[11] Y. Zhang, L. Ying, Z. Wang, Y. Wang, Q. Xu, C. Li, Unexpected hydrophobic to hydrophilic transition of PET fabric treated in a deep eutectic solvent of choline chloride and oxalic acid, Polym. (Guildf.) 234 (2021) 124246, https://doi.org/10.1016/j.polymer.2021.124246.
[12] R. Nisticò, Polyethylene terephthalate (PET) in the packaging industry, Polym. Test. 90 (2020) 106707, https://doi.org/10.1016/j.polymertesting.2020.106707.
[13] V. Dhaka, S. Singh, A.G. Anil, T.S. Sunil Kumar Naik, S. Garg, J. Samuel, M. Kumar, P.C. Ramamurthy, J. Singh, Occurrence, toxicity and remediation of polyethylene terephthalate plastics. a review, Environ. Chem. Lett. 20 (2022) 1777–1800, https://doi.org/10.1007/s10311-021-01384-8.
[14] A.K. Singh, R. Bedi, B.S. Kaith, Composite materials based on recycled polyethylene terephthalate and their properties – a comprehensive review, Compos. Part B Eng. 219 (2021) 108928, https://doi.org/10.1016/j.compositesb.2021.108928.
[15] T. Sang, C.J. Wallis, G. Hill, G.J.P. Britovsek, Polyethylene terephthalate degradation under natural and accelerated weathering conditions, Eur. Polym. J. 136 (2020) 109873, https://doi.org/10.1016/j.eurpolymj.2020.109873.
[16] R. Zhang, X. Ma, X. Shen, Y. Zhai, T. Zhang, C. Ji, J. Hong, PET bottles recycling in China: An LCA coupled with LCC case study of blanket production made of waste PET bottles, J. Environ. Manag. 260 (2020) 110062, https://doi.org/10.1016/j.jenvman.2019.110062.
[17] M. Shanmugam, C. Chuaicham, A. Augustin, K. Sasaki, P.J.J. Sagayaraj, K. Sekar, Upcycling hazardous metals and PET waste-derived metal–organic frameworks: a review on recent progresses and prospects, N. J. Chem. 46 (2022) 15776–15794, https://doi.org/10.1039/D2NJ02481K.
[18] L. Karam, A. Miglio, S. Specchia, N. El Hassan, P. Massiani, J. Reboul, PET waste as organic linker source for the sustainable preparation of MOF-derived methane dry reforming catalysts, Mater. Adv. 2 (2021) 2750–2758, https://doi.org/10.1039/D0MA00984A.
[19] S.-H. Lo, D. Senthil Raja, C.-W. Chen, Y.-H. Kang, J.-J. Chen, C.-H. Lin, Waste polyethylene terephthalate (PET) materials as sustainable precursors for the synthesis of nanoporous MOFs, MIL-47, MIL-53(Cr, Al, Ga) and MIL-101(Cr), Dalt. Trans. 45 (2016) 9565–9573, https://doi.org/10.1039/C6DT01282E.
[20] A.M. Al-Enizi, M. Ubaidullah, J. Ahmed, T. Ahamad, T. Ahmad, S.F. Shaikh, M. Naushad, Synthesis of NiOx@NPC composite for high-performance supercapacitor via waste PET plastic-derived Ni-MOF, Compos. Part B Eng. 183 (2020) 107655, https://doi.org/10.1016/j.compositesb.2019.107655.
[21] E. Cho, S. Yong Lee, J.-W. Choi, S.-H. Kim, K.-W. Jung, Direct upcycling of polyethylene terephthalate (PET) waste bottles into α-Fe2O3 incorporated MIL-53 (Al) for the synthesis of Al2O3/Fe3O4-encapsulated magnetic carbon composite and efficient removal of non-steroidal anti-inflammatory drugs, Sep. Purif. Technol. 279 (2021) 119719, https://doi.org/10.1016/j.seppur.2021.119719.
[22] X. Dyosiba, J. Ren, N.M. Musyoka, H.W. Langmi, M. Mathe, M.S. Onyango, Preparation of value-added metal-organic frameworks (MOFs) using waste PET bottles as source of acid linker, Sustain. Mater. Technol. 10 (2016) 10–13, https://doi.org/10.1016/j.susmat.2016.10.001.

[23] M.C. Ribadeneyra, J. King, M.M. Titirici, P.Á. Szilágyi, A facile and sustainable one-pot approach to the aqueous and low-temperature PET-to-UiO-66(Zr) upcycling, Chem. Commun. 58 (2022) 1330–1333, https://doi.org/10.1039/D1CC06250F.
[24] P. He, Z. Hu, Z. Dai, H. Bai, Z. Fan, R. Niu, J. Gong, Q. Zhao, T. Tang, Mechanochemistry milling of waste poly(ethylene terephthalate) into metal–organic frameworks, ChemSusChem 16 (2023), https://doi.org/10.1002/cssc.202201935.
[25] W.P.R. Deleu, I. Stassen, D. Jonckheere, R. Ameloot, D.E. De Vos, Waste PET (bottles) as a resource or substrate for MOF synthesis, J. Mater. Chem. A. 4 (2016) 9519–9525, https://doi.org/10.1039/C6TA02381A.
[26] O. Semyonov, S. Chaemchuen, A. Ivanov, F. Verpoort, Z. Kolska, M. Syrtanov, V. Svorcik, M.S. Yusubov, O. Lyutakov, O. Guselnikova, P.S. Postnikov, Smart recycling of PET to sorbents for insecticides through in situ MOF growth, Appl. Mater. Today 22 (2021) 100910, https://doi.org/10.1016/j.apmt.2020.100910.
[27] O. Semyonov, D. Kogolev, G. Mamontov, E. Kolobova, A. Trelin, M.S. Yusubov, O. Guselnikova, P.S. Postnikov, Synergetic effect of UiO-66 and plasmonic AgNPs on PET waste support towards degradation of nerve agent simulant, Chem. Eng. J. 431 (2022) 133450, https://doi.org/10.1016/j.cej.2021.133450.
[28] R. Gulyaev, O. Semyonov, G.V. Mamontov, A.A. Ivanov, D.M. Ivanov, M. Kim, V. Švorčík, G. Resnati, T. Liao, Z. Sun, Y. Yamauchi, P.S. Postnikov, O. Guselnikova, Weak bonds, strong effects: enhancing the separation performance of UiO-66 toward chlorobenzenes via halogen bonding, ACS Mater. Lett. 5 (2023) 1340–1349, https://doi.org/10.1021/acsmaterialslett.2c01169.
[29] D. Kogolev, O. Semyonov, N. Metalnikova, M. Fatkullin, R.D. Rodriguez, P. Slepicka, Y. Yamauchi, O. Guselnikova, R. Boukherroub, P.S. Postnikov, Waste PET upcycling to conductive carbon-based composite through laser-assisted carbonization of UiO-66, J. Mater. Chem. A. 11 (2023) 1108–1115, https://doi.org/10.1039/D2TA08127J.
[30] M. Barakzehi, M. Montazer, F. Sharif, T. Norby, A. Chatzitakis, MOF-modified polyester fabric coated with reduced graphene oxide/polypyrrole as electrode for flexible supercapacitors, Electrochim. Acta 336 (2020) 135743, https://doi.org/10.1016/j.electacta.2020.135743.
[31] H. Zhang, X.-L. Zhou, L.-M. Shao, F. Lü, P.-J. He, Upcycling of PET waste into methane-rich gas and hierarchical porous carbon for high-performance supercapacitor by autogenic pressure pyrolysis and activation, Sci. Total Environ. 772 (2021) 145309, https://doi.org/10.1016/j.scitotenv.2021.145309.
[32] P. Athanasopoulos, A. Zabaniotou, Post-consumer textile thermochemical recycling to fuels and biocarbon: a critical review, Sci. Total Environ. 834 (2022) 155387, https://doi.org/10.1016/j.scitotenv.2022.155387.
[33] S. Chen, S. Fang, A.I. Lim, J. Bao, Y.H. Hu, 3D meso/macroporous carbon from MgO-templated pyrolysis of waste plastic as an efficient electrode for supercapacitors, Chemosphere 322 (2023) 138174, https://doi.org/10.1016/j.chemosphere.2023.138174.
[34] X. Liu, Y. Wen, X. Chen, T. Tang, E. Mijowska, Co-etching effect to convert waste polyethylene terephthalate into hierarchical porous carbon toward excellent capacitive energy storage, Sci. Total Environ. 723 (2020) 138055, https://doi.org/10.1016/j.scitotenv.2020.138055.
[35] Z. Fan, J. Ren, H. Bai, P. He, L. Hao, N. Liu, B. Chen, R. Niu, J. Gong, Shape-controlled fabrication of MnO/C hybrid nanoparticle from waste polyester for solar evaporation and thermoelectricity generation, Chem. Eng. J. 451 (2023) 138534, https://doi.org/10.1016/j.cej.2022.138534.
[36] Y. Wen, K. Kierzek, J. Min, X. Chen, J. Gong, R. Niu, X. Wen, J. Azadmanjiri, E. Mijowska, T. Tang, Porous carbon nanosheet with high surface area derived from waste poly(ethylene terephthalate) for supercapacitor applications, J. Appl. Polym. Sci. 137 (2020), https://doi.org/10.1002/app.48338.
[37] M. Ubaidullah, A.M. Al-Enizi, S. Shaikh, M.A. Ghanem, R.S. Mane, Waste PET plastic derived ZnO@NMC nanocomposite via MOF-5 construction for hydrogen and oxygen evolution reactions, J. King Saud. Univ. - Sci. 32 (2020) 2397–2405, https://doi.org/10.1016/j.jksus.2020.03.025.
[38] K.-W. Jung, J.-H. Kim, J.-W. Choi, Synthesis of magnetic porous carbon composite derived from metal-organic framework using recovered terephthalic acid from polyethylene terephthalate (PET) waste bottles as organic ligand and its potential as adsorbent for antibiotic tetracycline hydrochlo, Compos. Part B Eng. 187 (2020) 107867, https://doi.org/10.1016/j.compositesb.2020.107867.
[39] T. Ma, W. Wang, R. Wang, Thermal degradation and carbonization mechanism of Fe-based metal-organic frameworks onto flame-retardant polyethylene terephthalate, Polym. (Basel) 15 (2023) 224, https://doi.org/10.3390/polym15010224.
[40] G.-T. Xiang, N. Chen, B. Lu, J.-L. Xu, R.D. Rodriguez, E. Sheremet, Y.-D. Hu, J.-J. Chen, Flexible solid-state Zn-Co MOFs@MXene supercapacitors and organic ion hydrogel sensors for self-powered smart sensing applications, Nano Energy 118 (2023) 108936, https://doi.org/10.1016/j.nanoen.2023.108936.
[41] Y. Tang, H. Zheng, Y. Wang, W. Zhang, K. Zhou, Laser-induced annealing of metal–organic frameworks on conductive substrates for electrochemical water splitting, Adv. Funct. Mater. 31 (2021), https://doi.org/10.1002/adfm.202102648.
[42] W. Zhang, R. Li, H. Zheng, J. Bao, Y. Tang, K. Zhou, Laser-assisted printing of electrodes using metal–organic frameworks for micro-supercapacitors, Adv. Funct. Mater. 31 (2021), https://doi.org/10.1002/adfm.202009057.
[43] J. Xu, R. Wang, H. Jiang, X. Liu, L. An, S. Jin, B. Deng, W. Wu, G.J. Cheng, Magnetically aligned ultrafine cobalt embedded 3D porous carbon metamaterial by one-step ultrafast laser direct writing, Adv. Sci. 8 (2021), https://doi.org/10.1002/advs.202102477.
[44] D.Van Lam, V. Nguyen, E. Roh, Q. Ngo, W. Choi, J. Kim, H. Kim, H. Choi, S. Lee, Laser-induced graphitic carbon with ultrasmall nickel nanoparticles for efficient overall water splitting, Part. Part. Syst. Charact. 38 (2021), https://doi.org/10.1002/ppsc.202100119.
[45] W. Zhang, R. Li, H. Zheng, J. Bao, Y. Tang, K. Zhou, Laser-assisted printing of electrodes using metal–organic frameworks for micro-supercapacitors, Adv. Funct. Mater. 31 (2021) 2009057, https://doi.org/10.1002/adfm.202009057.
[46] W. Chaouch, F. Dieval, D. Le Nouen, A. Defoin, N. Chakfe, B. Durand, Nuclear magnetic resonance spectroscopy spectroscopic investigation of the aging mechanism of polyethylene terephthalate vascular prostheses, J. Appl. Polym. Sci. 113 (2009) 2813–2825, https://doi.org/10.1002/app.30089.
[47] G. Zhao, X. Dong, Y. Du, N. Zhang, G. Bai, D. Wu, H. Ma, Y. Wang, W. Cao, Q. Wei, Enhancing electrochemiluminescence efficiency through introducing atomically dispersed ruthenium in nickel-based metal–organic frameworks, Anal. Chem. 94 (2022) 10557–10566, https://doi.org/10.1021/acs.analchem.2c02334.
[48] F. Dubelley, E. Planes, C. Bas, E. Pons, B. Yrieix, L. Flandin, The hygrothermal degradation of PET in laminated multilayer, Eur. Polym. J. 87 (2017) 1–13, https://doi.org/10.1016/j.eurpolymj.2016.12.004.
[49] C. Sammon, J. Yarwood, N. Everall, An FT–IR study of the effect of hydrolytic degradation on the structure of thin PET films, Polym. Degrad. Stab. 67 (2000) 149–158, https://doi.org/10.1016/S0141-3910(99)00104-4.
[50] H. Chang, Y. Zhou, S. Zhang, X. Zheng, Q. Xu, CO 2 -Induced 2D Ni-BDC metal–organic frameworks with enhanced photocatalytic CO2 reduction activity, Adv. Mater. Interfaces 8 (2021), https://doi.org/10.1002/admi.202100205.
[51] L.L. Mguni, Y. Yao, J. Ren, X. Liu, D. Hildebrandt, Modulated synthesized Ni-based MOF with improved adsorptive desulfurization activity, J. Clean. Prod. 323 (2021) 129196, https://doi.org/10.1016/j.jclepro.2021.129196.
[52] L. Ai, N. Li, M. Chen, H. Jiang, J. Jiang, Photothermally boosted water splitting electrocatalysis by broadband solar harvesting nickel phosphide within a quasi-MOF, J. Mater. Chem. A. 9 (2021) 16479–16488, https://doi.org/10.1039/D1TA02995A.
[53] L. Xia, Q. Zhang, X. Zhuang, S. Zhang, C. Duan, X. Wang, B. Cheng, Hot-pressed wet-laid polyethylene terephthalate nonwoven as support for separation membranes, Polym. (Basel) 11 (2019) 1547, https://doi.org/10.3390/polym11101547.
[54] D. Zhu, J. Liu, L. Wang, Y. Du, Y. Zheng, K. Davey, S.-Z. Qiao, A 2D metal–organic framework/Ni(OH) 2 heterostructure for an enhanced oxygen evolution reaction, Nanoscale 11 (2019) 3599–3605, https://doi.org/10.1039/C8NR09680E.
[55] A. Lipovka, I. Petrov, M. Fatkullin, G. Murastov, A. Ivanov, N.E. Villa, S. Shchadenko, A. Averkiev, A. Chernova, F. Gubarev, M. Saqib, W. Sheng, J.-J. Chen, O. Kanoun, I. Amin, R.D. Rodriguez, E. Sheremet, Photoinduced flexible graphene/polymer nanocomposites: design, formation mechanism, and properties engineering, Carbon N. Y. 194 (2022) 154–161, https://doi.org/10.1016/j.carbon.2022.03.039.
[56] D.A. Sokolov, C.M. Rouleau, D.B. Geohegan, T.M. Orlando, Excimer laser reduction and patterning of graphite oxide, Carbon N. Y. 53 (2013) 81–89, https://doi.org/10.1016/j.carbon.2012.10.034.
[57] V. Strong, S. Dubin, M.F. El-Kady, A. Lech, Y. Wang, B.H. Weiller, R.B. Kaner, Patterning and electronic tuning of laser scribed graphene for flexible all-carbon devices, ACS Nano 6 (2012) 1395–1403, https://doi.org/10.1021/nn204200w.
[58] E. Kymakis, K. Savva, M.M. Stylianakis, C. Fotakis, E. Stratakis, Flexible organic photovoltaic cells with in situ nonthermal photoreduction of spin-coated graphene oxide electrodes, Adv. Funct. Mater. 23 (2013) 2742–2749, https://doi.org/10.1002/adfm.201202713.
[59] J. Ren, C. Wang, X. Zhang, T. Carey, K. Chen, Y. Yin, F. Torrisi, Environmentally-friendly conductive cotton fabric as flexible strain sensor based on hot press reduced graphene oxide, Carbon N. Y. 111 (2017) 622–630, https://doi.org/10.1016/j.carbon.2016.10.045.
[60] T. Raza, M.K. Tufail, A. Ali, A. Boakye, X. Qi, Y. Ma, A. Ali, L. Qu, M. Tian, Wearable and flexible multifunctional sensor based on laser-induced graphene for the sports monitoring system, ACS Appl. Mater. Interfaces 14 (2022) 54170–54181, https://doi.org/10.1021/acsami.2c14847.
[61] L. Cheng, G. Fang, L. Wei, W. Gao, X. Wang, Z. Lv, W. Xu, C. Ding, H. Wu, W. Zhang, A. Liu, Laser-induced graphene strain sensor for conformable lip-reading recognition and human–machine interaction, ACS Appl. Nano Mater. 6 (2023) 7290–7298, https://doi.org/10.1021/acsanm.3c00410.
[62] S. Hong, J. Kim, S. Jung, J. Lee, B.S. Shin, Surface morphological growth characteristics of laser-induced graphene with UV pulsed laser and sensor applications, ACS Mater. Lett. 5 (2023) 1261–1270, https://doi.org/10.1021/acsmaterialslett.2c01222.
[63] H. Liu, K. Chen, R. Wu, S. Pan, C. Zhang, Laser-induced graphene-based flexible substrate with photothermal conversion and photoresponse performance on polyimide film, ACS Appl. Mater. Interfaces 15 (2023) 46550–46558, https://doi.org/10.1021/acsami.3c10729.
[64] Y.C. Guan, Y.W. Fang, G.C. Lim, H.Y. Zheng, M.H. Hong, Fabrication of laser-reduced graphene oxide in liquid nitrogen environment, Sci. Rep. 6 (2016) 28913, https://doi.org/10.1038/srep28913.
[65] I.I. Bobrinetskiy, A.V. Emelianov, S.A. Smagulova, I.A. Komarov, N. Otero, P. M. Romero, Laser direct 3D patterning and reduction of graphene oxide film on polymer substrate, Mater. Lett. 187 (2017) 20–23, https://doi.org/10.1016/j.matlet.2016.10.073.
[66] R. Rahimi, M. Ochoa, W. Yu, B. Ziaie, Highly stretchable and sensitive unidirectional strain sensor via laser carbonization, ACS Appl. Mater. Interfaces 7 (2015) 4463–4470, https://doi.org/10.1021/am509087u.
[67] A.R. Cardoso, A.C. Marques, L. Santos, A.F. Carvalho, F.M. Costa, R. Martins, M.G. F. Sales, E. Fortunato, Molecularly-imprinted chloramphenicol sensor with laser-induced graphene electrodes, Biosens. Bioelectron. 124–125 (2019) 167–175, https://doi.org/10.1016/j.bios.2018.10.015.

[68] L. Cao, S. Zhu, B. Pan, X. Dai, W. Zhao, Y. Liu, W. Xie, Y. Kuang, X. Liu, Stable and durable laser-induced graphene patterns embedded in polymer substrates, Carbon N. Y. 163 (2020) 85–94, https://doi.org/10.1016/j.carbon.2020.03.015.
[69] J. Edberg, R. Brooke, O. Hosseinaei, A. Fall, K. Wijeratne, M. Sandberg, Laser-induced graphitization of a forest-based ink for use in flexible and printed electronics, NPJ Flex. Electron. 4 (2020) 17, https://doi.org/10.1038/s41528-020-0080-2.
[70] R.D. Rodriguez, S. Shchadenko, G. Murastov, A. Lipovka, M. Fatkullin, I. Petrov, T. Tran, A. Khalelov, M. Saqib, N.E. Villa, V. Bogoslovskiy, Y. Wang, C. Hu, A. Zinovyev, W. Sheng, J. Chen, I. Amin, E. Sheremet, Ultra-robust flexible electronics by laser-driven polymer-nanomaterials integration, Adv. Funct. Mater. 31 (2021), https://doi.org/10.1002/adfm.202008818.
[71] M.-S. Wu, W.-H. Hsu, Nickel nanoparticles embedded in partially graphitic porous carbon fabricated by direct carbonization of nickel-organic framework for high-performance supercapacitors, J. Power Sources 274 (2015) 1055–1062, https://doi.org/10.1016/j.jpowsour.2014.10.133.
[72] A. Furlan, J. Lu, L. Hultman, U. Jansson, M. Magnuson, Crystallization characteristics and chemical bonding properties of nickel carbide thin film nanocomposites, J. Phys. Condens. Matter 26 (2014) 415501, https://doi.org/10.1088/0953-8984/26/41/415501.
[73] Y. Wu, Z. Huang, H. Jiang, C. Wang, Y. Zhou, W. Shen, H. Xu, H. Deng, Facile synthesis of uniform metal carbide nanoparticles from metal–organic frameworks by laser metallurgy, ACS Appl. Mater. Interfaces 11 (2019) 44573–44581, https://doi.org/10.1021/acsami.9b13864.
[74] R.D. Rodriguez, S. Shchadenko, G. Murastov, A. Lipovka, M. Fatkullin, I. Petrov, T. Tran, A. Khalelov, M. Saqib, N.E. Villa, V. Bogoslovskiy, Y. Wang, C. Hu, A. Zinovyev, W. Sheng, J. Chen, I. Amin, E. Sheremet, Ultra-robust flexible electronics by laser-driven polymer-nanomaterials integration, Adv. Funct. Mater. 31 (2021) 2008818, https://doi.org/10.1002/adfm.202008818.
[75] M.-C. Liu, Y.-M. Hu, W.-Y. An, Y.-X. Hu, L.-Y. Niu, L.-B. Kong, L. Kang, Construction of high electrical conductive nickel phosphide alloys with controllable crystalline phase for advanced energy storage, Electrochim. Acta 232 (2017) 387–395, https://doi.org/10.1016/j.electacta.2017.02.169.
[76] A.I.A. Soliman, A.-M.A. Abdel-Wahab, H.N. Abdelhamid, Hierarchical porous zeolitic imidazolate frameworks (ZIF-8) and ZnO@N-doped carbon for selective adsorption and photocatalytic degradation of organic pollutants, RSC Adv. 12 (2022) 7075–7084, https://doi.org/10.1039/D2RA00503D.
[77] Y. Hu, H. Yao, Q. Liao, T. Lin, H. Cheng, L. Qu, The promising solar-powered water purification based on graphene functional architectures, EcoMat 4 (2022), https://doi.org/10.1002/eom2.12205.
[78] A.K. Pathak, M. Borah, A. Gupta, T. Yokozeki, S.R. Dhakate, Improved mechanical properties of carbon fiber/graphene oxide-epoxy hybrid composites, Compos. Sci. Technol. 135 (2016) 28–38, https://doi.org/10.1016/j.compscitech.2016.09.007.
[79] Y. Han, Y. Han, X. Zhang, L. Li, C. Zhang, J. Liu, G. Lu, H.-D. Yu, W. Huang, Fish Gelatin based triboelectric nanogenerator for harvesting biomechanical energy and self-powered sensing of human physiological signals, ACS Appl. Mater. Interfaces 12 (2020) 16442–16450, https://doi.org/10.1021/acsami.0c01061.
[80] A. Lipovka, M. Fatkullin, S. Shchadenko, I. Petrov, A. Chernova, E. Plotnikov, V. Menzelintsev, S. Li, L. Qiu, C. Cheng, R.D. Rodriguez, E. Sheremet, Textile electronics with laser-induced graphene/polymer hybrid fibers, ACS Appl. Mater. Interfaces 15 (2023) 38946–38955, https://doi.org/10.1021/acsami.3c06968.
[81] H. Yang, S. Ji, I. Chaturvedi, H. Xia, T. Wang, G. Chen, L. Pan, C. Wan, D. Qi, Y.-S. Ong, X. Chen, Adhesive biocomposite electrodes on sweaty skin for long-term continuous electrophysiological monitoring, ACS Mater. Lett. 2 (2020) 478–484, https://doi.org/10.1021/acsmaterialslett.0c00085.
[82] Z. Lou, S. Chen, L. Wang, R. Shi, L. Li, K. Jiang, D. Chen, G. Shen, Ultrasensitive and ultraflexible e-skins with dual functionalities for wearable electronics, Nano Energy 38 (2017) 28–35, https://doi.org/10.1016/j.nanoen.2017.05.024.
[83] J. Cao, C. Lu, J. Zhuang, M. Liu, X. Zhang, Y. Yu, Q. Tao, Multiple hydrogen bonding enables the self-healing of sensors for human–machine interactions, Angew. Chem. 129 (2017) 8921–8926, https://doi.org/10.1002/ange.201704217.